Materials & Design 237 (2024) 112589

Contents lists available at ScienceDirect

Materials & Design

journal homepage: www.elsevier.com/locate/matdes

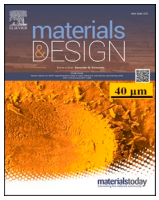

Effects of Y and Ho doping on microstructure evolution during oxidation of extraordinary stable Hf-B-Si-Y/Ho-C-N films up to 1500 °C

J.C. Jiang [a], Y. Shen [a], P. Zeman [b], M. Procházka [b], J. Vlček [b], E.I. Meletis [a,*]

[a] Department of Materials Science and Engineering, The University of Texas at Arlington, Arlington 76019 TX, USA
[b] Department of Physics and NTIS- European Centre of Excellence, University of West Bohemia, Univerzitní 8, 30614 Plzeň, Czech Republic

ARTICLE INFO

Keywords:
Hard coating
High temperature oxidation resistance
Transmission electron microscopy
X-ray diffraction
Electron diffraction

ABSTRACT

Hard, and optically transparent amorphous $Hf_6B_{12}Si_{29}Y_2C_2N_{45}$ and $Hf_5B_{13}Si_{25}Ho_3C_2N_{48}$ films were prepared by reactive pulsed dc magnetron co-sputtering and annealed up to 1500 °C in air. The evolved microstructures were studied by X-ray diffraction and transmission electron microscopy to understand the Y- and Ho– doping effects on thermal stability and oxidation behavior. A three-layered microstructure developed in both annealed films. A fully oxidized layer formed at the top surface consisting of cubic fluorite $Hf(Y/Ho)O_2$ nanoparticles embedded in an amorphous SiO_x-based matrix. The oxide layer is about 36 % thinner compared to undoped films with similar composition [1]. A recrystallized structure formed at the bottom of both films composed mainly of Hf(Y/Ho)N and α-/β-Si_3N_4. All Hf(Y/Ho)N in the middle layer was oxidized producing vertically oriented $Hf(Y/Ho)O_2$ nanocolumns surrounded by Si_3N_4 nanocrystalline. The Y- and Ho– doping found to stabilize the cubic fluoride oxide structure and promoted its (1 1 1) columnar texture. The oxidation mechanism of Si_3N_4 nanodomains occurs via formation of β-SiO_2 first followed by its transformation to amorphous SiO_x. It is suggested that substitution of Hf^{4+} with Y^{3+} and Ho^{3+} ions within the $Hf(Y/Ho)O_2$ formed an anion vacancy defect structure to preserve charge neutrality affecting the oxidation mechanism in the doped films.

1. Introduction

HfB_2- and ZrB_2-based ultra-high temperature ceramics possess desirable properties of high hardness, high melting point, superior oxidation resistance, and good thermal stability. These ceramics are potential candidates for high temperature applications such as critical frame structure of hypersonic vehicles, high-speed cutting tools, refractory linings and high-temperature electrodes and microelectronics wherein the operation temperatures are well above 1000 °C [2–17]. These materials have attracted tremendous attention and have been extensively studied in the recent years. It has been found that their high temperature oxidation resistance is due to the formation of an oxide layer, consisting of a metal oxide skeleton in a silicon oxide matrix providing excellent protection against further oxygen permeation [7,10–12,15,18–22]. We have recently reported on Hf–B–Si–C films exhibiting high hardness, high electrical conductivity, and good oxidation resistance up to 800 °C [23] and on high-temperature oxidation resistant Si-B-C-N films exhibiting superior oxidation resistance and thermal stability up to 1700 °C [18,22,24]. Therefore, incorporating nitrogen into the Hf-B-Si-C system can play an important role in improving the high temperature oxidation resistance of these ceramic films.

Most recently, we have published works on a series of Hf-B-Si-C-N films with variations in N and Si content in the film composition. These films exhibit superior high-temperature stability and oxidation resistance at temperatures up to 1600 °C and are promising candidates for high-temperature protection of optical and optoelectronic devices or capacitive sensors used in harsh environments [1,25–27]. A comprehensive microstructure analysis utilizing high-resolution transmission electron microscopy (HRTEM) and selected-area electron diffraction (SAED) was conducted to understand the relationship between film composition and microstructure evolution at high temperatures, the effect of the Si:B ratio in view of their N content on the evolved microstructure and the oxidation mechanism of Hf-B-Si-C-N films. It was found that after being annealed up to 1500 °C in air, the original amorphous Hf-B-Si-C-N films developed into a layered structure with a fully oxidized top layer followed by a bottom layer with a structure dependent on the N content and Si:B ratio [1,25,27]. The bottom layer in high N (>45 at.%) and low Si:B ratio (~1:1) films remains amorphous. However, in low N or high Si:B (~3:1) ratio films, the bottom layer

* Corresponding author.
E-mail address: meletis@uta.edu (E.I. Meletis).

https://doi.org/10.1016/j.matdes.2023.112589
Received 7 October 2023; Received in revised form 29 November 2023; Accepted 15 December 2023
Available online 16 December 2023

partially recrystallizes forming HfB_2, HfN and Si_3N_4. In films with high N and high Si:B ratio, the bottom layer is mainly amorphous with presence of short range ordered structures.

Recent reports have shown that rare-earth silicates RE_2SiO_5 (Re = Y, Yb, Ho, etc.) can form a more stable protective barrier layer than pure silica in hot sections of gas turbine engines by limiting reaction with high-temperature steam [28–32]. We recently investigated the effect of a small addition (2 ~ 3 at.%) of Y or Ho in Hf-B-Si-C-N on the film properties [33]. The $Hf_6B_{12}Si_{29}Y_2C_2N_{45}$ and $Hf_5B_{13}Si_{25}Ho_3C_2N_{48}$ films were found to exhibit enhanced high-temperature oxidation resistance and thermal stability compared to their undoped counterpart. In the present study, we investigated the microstructure evolution of the $Hf_6B_{12}Si_{29}Y_2C_2N_{45}$ and $Hf_5B_{13}Si_{25}Ho_3C_2N_{48}$ films after annealing up to 1500 °C in air. A comprehensive TEM microstructure analysis was conducted to understand the effects of Y- and Ho– doping on the evolved microstructure and the oxidation mechanism of these extraordinary stable Hf–B–Si–Y/Ho–C–N films.

2. Experimental

Hf–B–Si–Y/Ho–C–N films were deposited by reactive pulsed dc magnetron co-sputtering of a target (127 × 254 mm^2) consisting of a B_4C plate overlapped by Hf, Si and Y or Ho stripes with the fixed 15 % Hf + 50 % Si + 5 % Hf/Y/Ho fractions in the target erosion area. The magnetron was driven by a pulsed dc Rübig MP 120 power supply operating at a repetition frequency of 10 kHz and an average target power of 500 W in a period with a fixed 50 μs negative-voltage pulse length and short-lived high positive voltage overshoots (higher than 200 V, as shown and discussed in the reported work [33]. The base pressure before each deposition was lower than 1 × 10^{-3} Pa. The total pressure of an argon-nitrogen mixture used for the depositions was 0.5 Pa with a nitrogen fraction of 25 %. The films were deposited onto Si(1 0 0), 6H-SiC and Cu substrates. The SiC substrate was used for annealing experiments above 1300 °C (to avoid melting of the Si substrate) and the Cu substrate for DSC analysis. No significant effect of the substrate type on the structure and the properties of the films was observed. The target-to-substrate distance was set to 100 mm. The substrates were held at a floating potential and the substrate temperature was 450 °C.

The thickness of the films was measured by a Veeco Dektak 8 Stylus profilometer with a vertical resolution of 0.75 nm. The elemental composition of the films was determined by the Rutherford backscattering spectrometry (RBS) and the elastic recoil detection (ERD) methods. The contents of Hf, B, Si, Y, Ho, C, N, Zr, O and Ar were measured by RBS, while the content of H by ERD. Regarding the constitutive elements (Hf, B, Si, Y/Ho, C, N), the maximum measurement error is 3 at.%. Regarding other elements detected in the film (Zr as an impurity of the Hf stripes, H, O and Ar), their total content does not exceed 4 at.%.

The mass changes of the Hf–B–Si–Y/Ho–C–N films on the SiC substrates during dynamical annealing were measured by thermogravimetry (TG) using a symmetrical high-resolution Setaram TAG 2400 system with an accuracy of ± 1 μg. The films with a size of 1 × 1 cm^2 were annealed in air at a flow rate of 1 l/h from room temperature up to 1500 °C, at a heating rate of 10 °C/min and cooling rate of 30 °C/min.

The crystallographic structure of the annealed films was first studied by X-ray diffraction (XRD) in a Bruker D8 Advance Diffractometer using a Cu Kα radiation at an applied voltage of 40 kV and current of 40 mA. Phase analysis was performed in a grazing incidence mode with a glancing angle of 5°, 2θ range from 10° to 62° and step size of 0.01°. Plan-view TEM samples were prepared by mechanical grinding and polishing, followed by dimpling using a Gatan Model 656 dimple grinder and Ar-ion milling in a Gatan Model 691 precision ion polishing system (PIPS). Cross-section TEM samples were also prepared using focus-ion beam (FIB) in a FEI Strata 400 dual-beam system and final cleaned by PIPS. Selected-area electron diffraction patterns, TEM and HRTEM images were recorded in a Hitachi H-9500 electron microscope operated at 300 keV with a point resolution of 0.18 nm.

3. Results

3.1. XRD analysis

Fig. 1 presents the XRD spectra of the as-deposited [33] and the annealed Hf–B–Si–Y/Ho–C–N films in air to 1500 °C using low-angle diffraction to avoid the excessive signal from the SiC substrate. The as-deposited films possess a pure amorphous structure. The spectra of both annealed films present weak peaks (100), (101), (110), (200), (202) and (222) of hexagonal Si_3N_4 (h-Si_3N_4, PDF#05–5074, hexagonal, $\boldsymbol{a}$ = 7.753 Å, $\boldsymbol{c}$ = 5.618 Å, $P3_1c$) [38] at 13.15°, 20.62°, 23.12°, 26.81°, 41.79° and 57.70°, respectively. In the XRD spectrum of the annealed $Hf_6B_{12}Si_{29}Y_2C_2N_{45}$ film, major peaks at 30.07°, 34.82°, 50.10° and 59.54° with a d-spacing of 2.969 Å, 2.574 Å, 1.820 Å and 1.551 Å, are respectively close to (111), (200), (220), and (311) of hafnium yttrium oxide $Hf_2Y_2O_7$ (HYO) (PDF#24–1406, a = 5.201 Å, $Fm\bar{3}m$) [34,35]. Similarly, the major peaks in the spectrum of $Hf_5B_{13}Si_{25}Ho_3C_2N_{48}$ at 29.98°, 34.71°, 49.96° and 59.44° with a d-spacing of 2.978 Å, 2.582 Å, 1.824 Å and 1.554 Å, are respectively close to (111), (200), (220), and (311) of hafnium holmium oxide $Hf_2Ho_2O_7$ (HHO) (PDF#24–0473, a = 5.206 Å, $Fm\bar{3}m$) [34]. Due to the small Y and Ho additions to the present films, a Hf/(Y/Ho) ratio higher than 1 is expected in the hafnium oxides along with a variation in the lattice parameter. These oxides can be represented as $Hf_{1-x}Y_xO_{2-x/2}$ (HYO) and $Hf_{1-x}Ho_xO_{2-x/2}$ (HHO), respectively. It is interesting to note that both H(Y/H)O oxide phases exhibit a cubic structure in contrast to the monoclinic or orthorhombic structure previously observed for the HfO_2 phase in the annealed undoped Hf-B-Si-C-N films [1,25,27]. Finally, both films show the presence of face centered cubic (fcc) HfCN (PDF#2–2469, a = 4.586 Å, $Fm\bar{3}m$) [34] with the (111) reflection being at the left shoulder of the (200) H(Y/H)O peak and a (200) peak at 39.75° with a d-spacing of 2.26 Å.

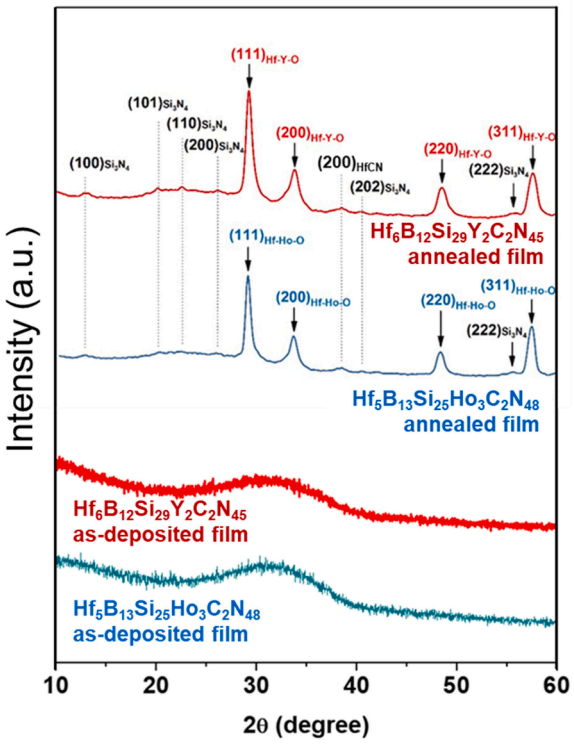

Fig. 1. (a) Low-angle XRD spectra of the as-deposited and annealed $Hf_6B_{12}Si_{29}Y_2C_2N_{45}$ and $Hf_5B_{13}Si_{25}Ho_3C_2N_{48}$ films in air to 1500 °C.

3.2. TEM studies

Microstructure of annealed $Hf_6B_{12}Si_{29}Y_2C_2N_{45}$ film.

3.2.1. Overall film structure

Fig. 2(a) shows a cross-section TEM image of the annealed $Hf_6B_{12}Si_{29}Y_2C_2N_{45}$ film presenting a clear multi-layered structure of: (i) a ~ 185 nm thick nanocomposite oxide layer (OL) with spherical nanoparticles dispersed in a rather amorphous SiO_x-based matrix on the top surface followed by (ii) a ~ 500 nm thick transition layer (TL) and (iii) a ~ 1350 nm thick graded recrystallized layer (RL) underneath. The total thickness of the annealed $Hf_6B_{12}Si_{29}Y_2C_2N_{45}$ film is 2035 nm. X-ray energy-dispersive spectroscopy (EDS) analysis shows that the spherical nanoparticles in the top OL show only presence of Hf, Y, and O, Fig. 2(b), suggesting that most of the Y is incorporated in the HYO nanoparticles. EDS analysis from the matrix presents only Si and O from amorphous SiO_x. EDS spectra from the bottom of the graded RL present mainly Si, Hf, Y, and N and a small amount of O towards the top of the RL. The O content increased along the thickness of the RL. It is noted though that EDS is simply not able to capture B due to of its low photon energy (0.185 keV).

3.2.2. Microstructure of the top oxide layer

Fig. 3(a) presents a zoom-in cross-section TEM image of the top OL in the annealed $Hf_6B_{12}Si_{29}Y_2C_2N_{45}$ film exhibiting a similar microstructure to that of Hf-B-Si-C-N film reported previously [1,25,27]. A clear interface is evident at the bottom of Fig. 3(a) showing the transition between the OL and TL. Fig. 3(b) shows a plan-view TEM image of the OL in the annealed $Hf_6B_{12}Si_{29}Y_2C_2N_{45}$ film obtained by removing the bottom layers and substrate presenting a typical microstructure of the OL over a much larger area of the film plane. The spherical nanoparticles are composed of Hf, Y and O (Fig. 2(b)) and have a size varying from ~ 20 nm to ~ 160 nm. They are well-dispersed in a SiO_x-based amorphous matrix. Fig. 3(c) is a SAED pattern taken from the top OL in a plan-view TEM foil presenting four rings composed of sharp diffraction spots. The diffraction rings I, II, III, and IV have a lattice spacing of 2.99 Å, 2.59 Å, 1.83 Å and 1.56 Å, which can be identified as the (111), (200), (220), and (311), respectively of a hafnia yttria fluorite phase $Hf_{1-x}Y_xO_{2-x/2}$ ($Fm\bar{3}m$, a = 5.18 Å) [35]. As noted earlier, the lattice constant of this oxide is somewhat smaller than that of $Hf_2Y_2O_7$ (a = 5.201 Å) due to its lower Y content.

Fig. 3(d) shows a nanobeam electron diffraction (NBED) pattern taken from particle X in Fig. 3(a) exhibiting the [110] zone diffraction pattern of the fluorite phase $Hf_{1-x}Y_xO_{2-x/2}$. Fig. 3(e) and (f) exhibit NBED patterns taken from particles Y and Z in Fig. 3(b) exhibiting the [001] and [11$\bar{2}$] zone diffraction pattern of the fluorite phase $Hf_{1-x}Y_xO_{2-x/2}$, respectively. The SAED and NBED analysis demonstrate that the spherical $Hf_{1-x}Y_xO_{2-x/2}$ nanoparticles have a fluorite type structure, different from that of the previously observed HfO_2 nanoparticles that have a monoclinic, orthorhombic, and/or tetragonal structure [1,25,27]. Fig. 3(g) presents a HRTEM image of a part of a $Hf_{1-x}Y_xO_{2-x/2}$ nanoparticle oriented along the [11$\bar{2}$] of the fluorite type structure. The image provides further evidence for the formation of fluorite $Hf_{1-x}Y_xO_{2-x/2}$ nanoparticles along with a seamless interface with the amorphous SiO_x matrix in the annealed $Hf_6B_{12}Si_{29}Y_2C_2N_{45}$ film.

3.2.3. Microstructure of the transition layer

The TL in Fig. 2(a) appears as a complex of vertically oriented columnar structures, like that observed in the annealed $Hf_6B_{10}Si_{31}C_2N_{50}$ and $Hf_7B_{10}Si_{32}C_2N_{44}$ films [1]. A plan-view TEM image of TL, obtained by removing the top OL and the bottom RL layer and substrate, is shown in Fig. 4(a). Dark island-like structures or streaks of particles are linked together forming borders to enclose bright domains. The dark borders have a thickness of ~ 10 nm, while the bright domains have a size of ~ 40–200 nm. EDS analysis showed that the dark structures contain only O, Hf and Y (top spectrum in Fig. 4(b)) and the bright regions consist of N, O, Si, Hf and Y (bottom spectrum in Fig. 4(b)).

A SAED pattern taken from the TL in Fig. 4(a) is shown in Fig. 4(c) presenting a complex pattern with several overlapping rings. The solid rings I, II, III, and IV have a lattice spacing of 2.96 Å, 2.57 Å, 1.81 Å, and 1.55 Å, and belong respectively to the (111), (200), (220), and (311) diffractions of the hafnia yttria fluorite phase $Hf_{1-x}Y_xO_{2-x/2}$ ($Fm\bar{3}m$, a = 5.13 Å) [39]. It is noticed that the $Hf_{1-x}Y_xO_{2-x/2}$ fluorite phase in the TL has a somewhat smaller lattice constant than that of the spherical particles in the OL (a = 5.18 Å). This is because the former has a higher Hf/Y ratio than the latter, which agrees with the results reported in the literature [35]. The lattice constant of $Hf_{1-x}Y_xO_{2-x/2}$ with x = 0.1 is about 5.13 Å and 5.18 Å for x = 0.3.

The diffraction rings 1, 2, 3, 4, 6, 7, 8, 9, and10 have a lattice spacing of 6.69 Å, 4.31 Å, 3.87 Å, 3.34 Å, 2.67 Å, 2.32 Å, 2.17 Å, 2.09 Å, and 1.60 Å, respectively. The diffractions 2, and 9 can be respectively identified as the (101), and (301) of α-Si_3N_4 (hexagonal, $\boldsymbol{a}$ = 7.753 Å, $\boldsymbol{c}$ = 5.618 Å, $P3_1c$) [36], while ring 6 as the (101) of β-Si_3N_4 (hexagonal, $\boldsymbol{a}$ = 7.6044 Å, $\boldsymbol{c}$ = 2.9063 Å, $P6_3/m$) [37]. The diffractions 1, 3, 4, 7, 8, and 10 can match either the (100), (110), (200), (211), (202), and

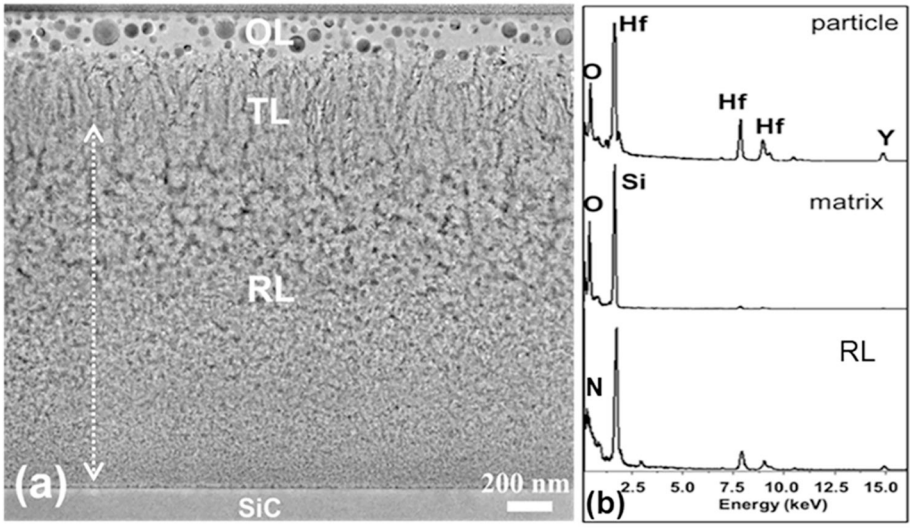

Fig. 2. (a) Cross-section TEM image of the annealed $Hf_6B_{12}Si_{29}Y_2C_2N_{45}$ film, and (b) EDS spectra taken from a spherical particle and matrix in the OL and from the bottom of the RL.

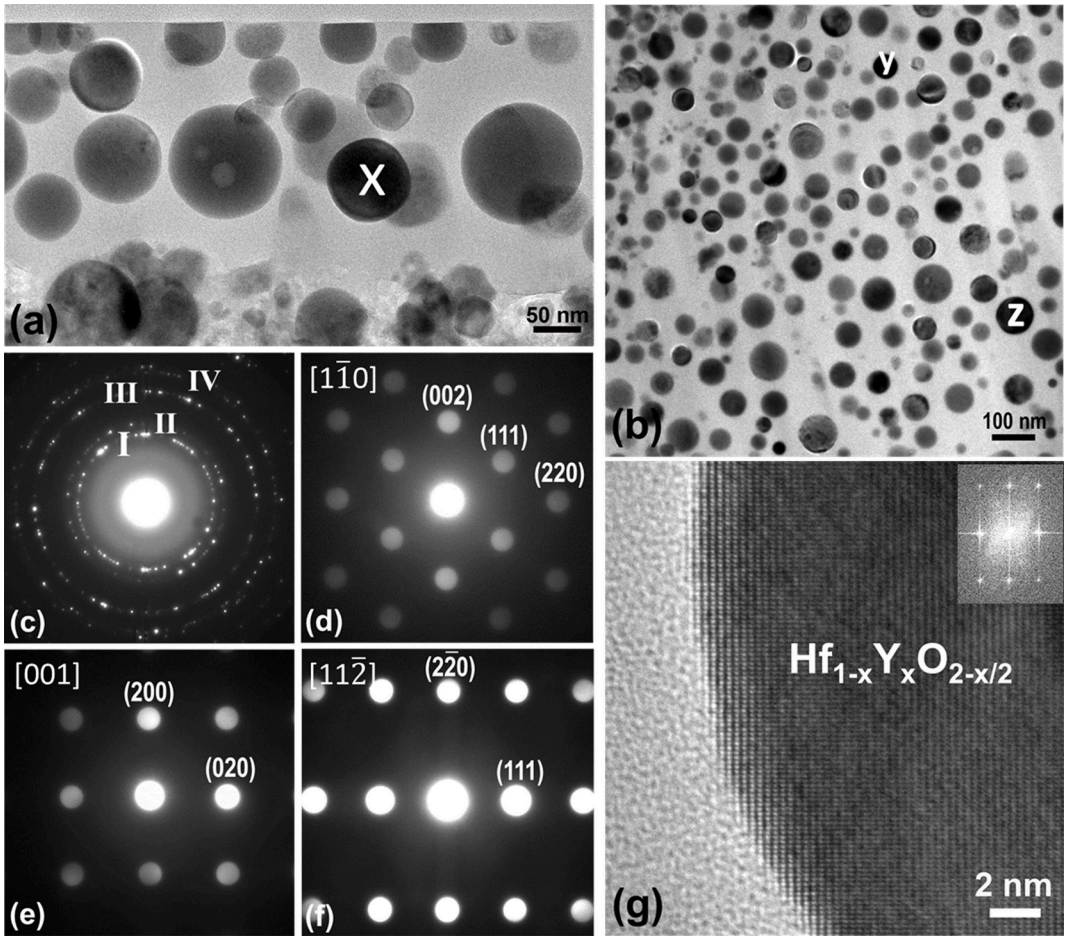

Fig. 3. (a) Zoom-in cross-section and (b) plan-view TEM image of the top OL in the annealed $Hf_6B_{12}Si_{29}Y_2C_2N_{45}$ film; (c) SAED pattern taken from the plan-view TEM foil shown in (b); (d), (e), and (f) nanobeam electron diffraction taken from nanoparticle x in (a), and Y and Z in (b), respectively; (g) HRTEM of a part of particle Z shown in (b).

(222) of α-Si_3N_4, or the (100), (110), (200), (111), (201) and (221) of β-Si_3N_4, respectively. Such overlapping of diffractions occurs due to the nearly same a-axis for both Si_3N_4 phases while the c-axis of α-Si_3N_4 is roughly double of that of β-Si_3N_4, as mentioned previously. It should also be noted that the (220) diffraction of $Hf_{1-x}Y_xO_{2-x/2}$ nearly overlaps with the (103) diffraction of α-Si_3N_4. The presence of unique (no overlapping) diffractions (101) and (301) of α-Si_3N_4 and (101) of β-Si_3N_4 indicates that both α-Si_3N_4 and β-Si_3N_4 were formed in the TL layer.

Fig. 4(d) is a SAED pattern taken from the cross-section of the TL layer in Fig. 2(a). As in Fig. 4(c), the SAED pattern shows the presence of Si_3N_4 and HYO. It is interesting to note that Ring I ((111) of HYO) in Fig. 4(d) exhibits a few strong diffraction spots indicative of a strong orientation preference of fluorite HYO in TL. Such a textured structure was confirmed by bright/dark field imaging (Fig. 4(e) and (f)) obtained by using diffraction spot I_1 in Fig. 4(d). The dark regions in Fig. 4(e) or the bright regions in Fig. 4(f) correspond to HYO structures that share a common crystallographic direction. The orientation preferred structures have a width of ~ 100 nm and a height of a few 100 nm, generated by closely joining the HYO nanostructures via sharing (111) planes. Thus, the oxidation process seems to involve some crystallographic aspect expressed with preferentially (111) oriented HYO grains. This feature was not observed in undoped Hf-Si-B-C-N films and can be attributed to the presence of yttrium in the oxide structure that results in crystallographic alignment and merging of HYO grains.

Fig. 5(a) shows a zoom-in plan-view TEM image exhibiting a cross-section view of the columnar structure in TL. The dark island-like structures were linked to form the column border which has a size of ~ 20–40 nm. The enclosed inner column region is filled with fine dark nanoparticles (~10 nm) dispersed in a bright matrix structure. Comprehensive analysis using EDS, NBED, and HRTEM demonstrated that the dark structures on the border and the dispersed fine nanoparticles within the inner column are fluorite HYO. The inner bright matrix appears either with a continuous solid morphology in some areas (such as "S" in Fig. 5(a)) or a discontinued grid structure in other locations (such as "G" in Fig. 5(a)).

Fig. 5(b) is plan-view HRTEM image from the border region in TL. The bright area on the low left corner in the image presents lattice fringes of α-Si_3N_4 (100) in the inner column. The dark nanoparticles on the border possess the same orientation exhibiting two-dimensional lattice image of fluorite HYO along the [110] zone axis. The inset fast Fourier transform (FFT) calculated from the entire HRTEM image in Fig. 5(b) presents strong (111), ($\bar{1}\bar{1}$1), and (002) of HYO that can be constructed as a single crystal diffraction pattern along the [1$\bar{1}$0] direction. Thus, the present evidence suggests that a preferred crystallographic element is involved in the formation of both the HYO and Si_3N_4.

Fig. 5(c) is a plan-view HRTEM image from a continuous structure within an inner column in TL presenting three fluorite HYO nanograins oriented with their [110] perpendicular to the image, implanted into a few Si_3N_4 grains that possess nearly the same [001] orientation. The HYO nanoparticles were directly attached to the Si_3N_4 without any transition layers or materials in between. The results indicate that the Si_3N_4 phase within the columnar area in TL could be either a single crystal grain with several HYO nanoprecipitates, or multi Si_3N_4 grains

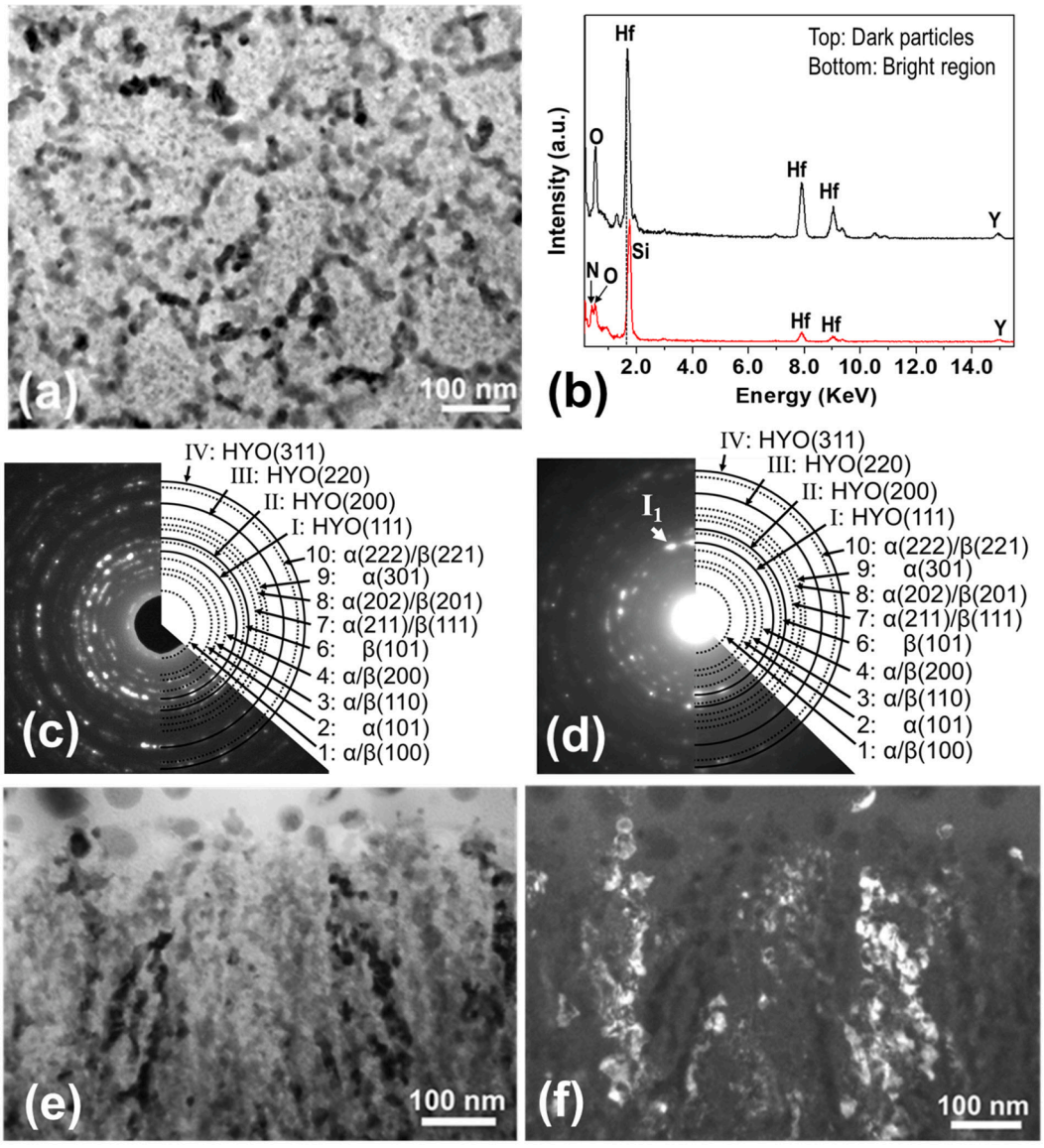

Fig. 4. (a) Plan-view TEM image of the TL in the annealed $Hf_6B_{12}Si_{29}Y_2C_2N_{45}$ film; (b) EDS spectra taken from the black particles on the boundaries and domains in (a); (c) SAED pattern taken from the TL layer in (a); (d) SAED pattern from the TL cross-section shown in Fig. 2(a); (e) Bright-field TEM image of a TL cross-section and (f) its corresponding dark-field image taken using diffraction I_1 in (d).

but possessing nearly the same [0 0 1] direction perpendicular to the film plane. The borders of the columnar structure were sealed with HYO nanoparticles, like those observed in the annealed $Hf_6B_{10}Si_{31}C_2N_{50}$ [1]. The present observations clearly show that the HYO domains at the border region, Fig. 5(b) or within the bright area, Fig. 5(c), form intimate interfaces with the Si_3N_4 structures.

Fig. 5(d) shows a plan-view HRTEM image from a discontinued grid location G in Fig. 5(a) presenting a HYO nanoparticle with (1 1 1) fringes on the right, a large α-Si_3N_4 grain in the center with presence of (1 0 1) lattice fringes and a small α-Si_3N_4 grain with (2 0 1) lattice fringes on the top-left. The α-Si_3N_4 grains were attached abruptly by three grid-like structures (G_1, G_2 and G_3) of a size of several nanometers. The grid-like structures appeared as amorphous crossed by a couple of curved β-SiO_2 (1 0 1) lattice fringes (shown by arrows) with a spacing of ~ 3.4 Å. Such evidence shows initial stages of oxidation of α-Si_3N_4 first to β-SiO_2 followed by formation of amorphous SiO_x as a result of the reaction of Si_3N_4 with O in TL.

Fig. 6(a) is a cross-section HRTEM image of TL in Fig. 2(a) presenting an atomic structure of the columnar region in a side view. The dark structure in the image corresponds to the borders of the columnar structure in TL exhibiting single oriented fluorite HYO (1 1 1) lattice fringes with a spacing of 2.96 Å. Such single oriented structure nearly extends to the entire TL layer providing further evidence of the formation of the strong orientation preferred fluorite HYO structure on the borders of the columnar structures. The areas between the borders are filled with disordered or non-crystalline characteristics which is due to the off orientation of the crystalline phases. The cross-section HRTEM images from different areas between the borders in the TL exhibit coexistence of a variety of phases. For example, it shows multi-oriented Si_3N_4 and HYO nanograins in Fig. 6(b), coexistence of [20$\bar{1}$] oriented α-Si_3N_4 crystalline with a couple of curved lattice fringes of β-quartz SiO_2 and amorphous SiO_x in Fig. 6(c), and [0 0 1] oriented fluorite HYO attached by the curved onion-like β-quartz SiO_2 (d-spacing of lattice fringes is 3.4 Å [1,25,27]) that encapsulated an amorphous SiO_x (α-SiO_2) core structure in Fig. 6(d). HRTEM images in Fig. 6(c) and (d) provide additional evidence for the onset of oxidation of Si_3N_4 in TL. The mechanism seems to involve initial transformation of Si_3N_4 to β-quartz SiO_2 that subsequently converts to amorphous SiO_x.

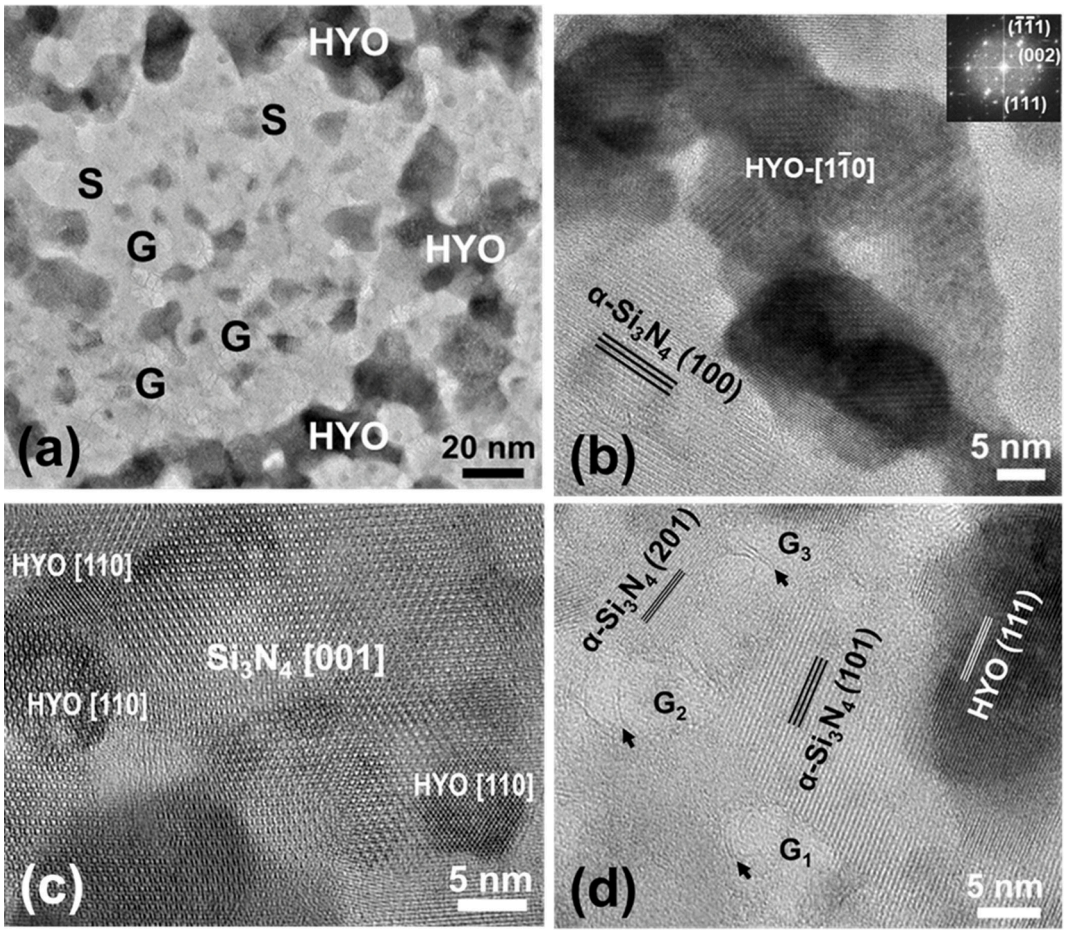

Fig. 5. (a) A zoom-in plan-view TEM image of TL in annealed $Hf_6B_{12}Si_{29}Y_2C_2N_{45}$ film, (b) HRTEM image of a region covering the border structure in TL in plan-view TEM foil, (c) HRTEM image taken from a continuous solid structure within the column shown in (a), and (d) HRTEM image taken from a discontinuous grid structure within the column shown in (a). (Curved β-SiO_2 lattice fringes are shown by arrows.).

3.2.4. Microstructure of the recrystallized layer

The RL underneath the TL appears as a graded fine dispersion of dark and bright domains, like the structure observed in the annealed $Hf_7B_{10}Si_{32}C_2N_{44}$ film [1]. Fig. 7(a - c) present zoom-in cross-section TEM images from the top, middle, and bottom sections within the RL in the annealed $Hf_6B_{12}Si_{29}Y_2C_2N_2$ film. The bottom section exhibits a composite of nearly even sized dark and bright domains with a typical size from a few to 15 nm, Fig. 7(c), indicative of the first stages of recrystallization. The middle section presents a similar structure to the bottom section but with a coarser domain size, of about ~ 20–30 nm, Fig. 7(b). The broadening of the domains in the middle section was accomplished by amalgamating several grains shown in Fig. 7(c). The top section possesses a honeycomb-like structure in which several dark domains in Fig. 7(b) merge together forming shells with a thickness of ~ 10–25 nm and the bright domains forming the bright core with a dimension of ~ 30–80 nm, Fig. 7(a). SAED patterns taken using a 300 nm diameter selected aperture from the top, middle and bottom sections of the RL are shown in Fig. 7(d-f) exhibiting very similar characteristics. They show the presence of α-Si_3N_4, β-Si_3N_4, HfCN, and HYO over the entire RL.

The diffraction spots γ with a lattice spacing of 2.62 Å shown in Fig. 7 (e) and (f) correspond to the (1 1 1) of fcc HfC_xN_{1-x} structure which is a solid solution of HfC (PDF #:39–1491, a = 4.638 Å, Fm3m) and HfN (PDF #:33–0592, a = 4.525 Å, Fm3m) [34]. It should be noted that the observed lattice spacing is somewhat smaller than that observed for HfCN previously (2.67 Å) [25]. The smaller lattice spacing is attributed to the participation of Y in the HfCN phase (denoted as HfYCN) of the present annealed $Hf_6B_{12}Si_{29}Y_2C_2N_{45}$ film. Such HfYCN diffractions were observed mostly in the bottom and middle sections (up to 850 nm above the substrate) and less often in the top section (850–1350 nm) of RL. This result manifests that HfYCN was formed in the bottom and middle section of the RL and gradually oxidized to HYO in the top section of RL (850–1350 nm above the substrate). The density and intensity of HfYCN diffraction (1 1 1) in Fig. 7(e) are reduced compared to those in Fig. 7(f) indicating the gradual reduction of HfYCN in the middle RL section compared to the bottom section. Thus, the evidence suggests that the HfYCN phase formed by recrystallization in the RL, gradually oxidized to HYO as the interface with TL is approached. Furthermore, this provides additional indirect evidence for the presence of Y in the HfCN structure which after oxidation was found by EDS, Fig. 2(b), to be present in the HYO phase.

Furthermore, four intense sharp diffraction spots are seen on ring I of (1 1 1) HYO in Fig. 7(d), which construct a near single crystal HYO [1 1 0] diffraction pattern from large grain(s). Meanwhile, the number of diffraction spots from (1 1 1), (2 0 0) and (2 2 0) of HYO on the rings I, II and III in Fig. 7(d) are accordingly reduced compared to Fig. 7(e) and (f). This also indicates that large HYO grains were developed in the top section of the RL due to fewer number of HYO grains included by the selected-area aperture for diffraction.

The detailed microstructure evolution along the film growth direction in the RL was studied by HRTEM. Fig. 8(a) is a representative HRTEM image from the top section of the RL (~850 nm above the substrate) showing presence of a [0 0 1] oriented HYO grain and a Si_3N_4 grain with the (2 0 0) lattice fringes of a spacing of 3.34 Å. The HYO and Si_3N_4 grains in this area are large and therefore only a part of these grains is shown in the image. A mixture of amorphous and β-SiO_2 with curved lattice fringes are also present between the Si_3N_4 and HYO

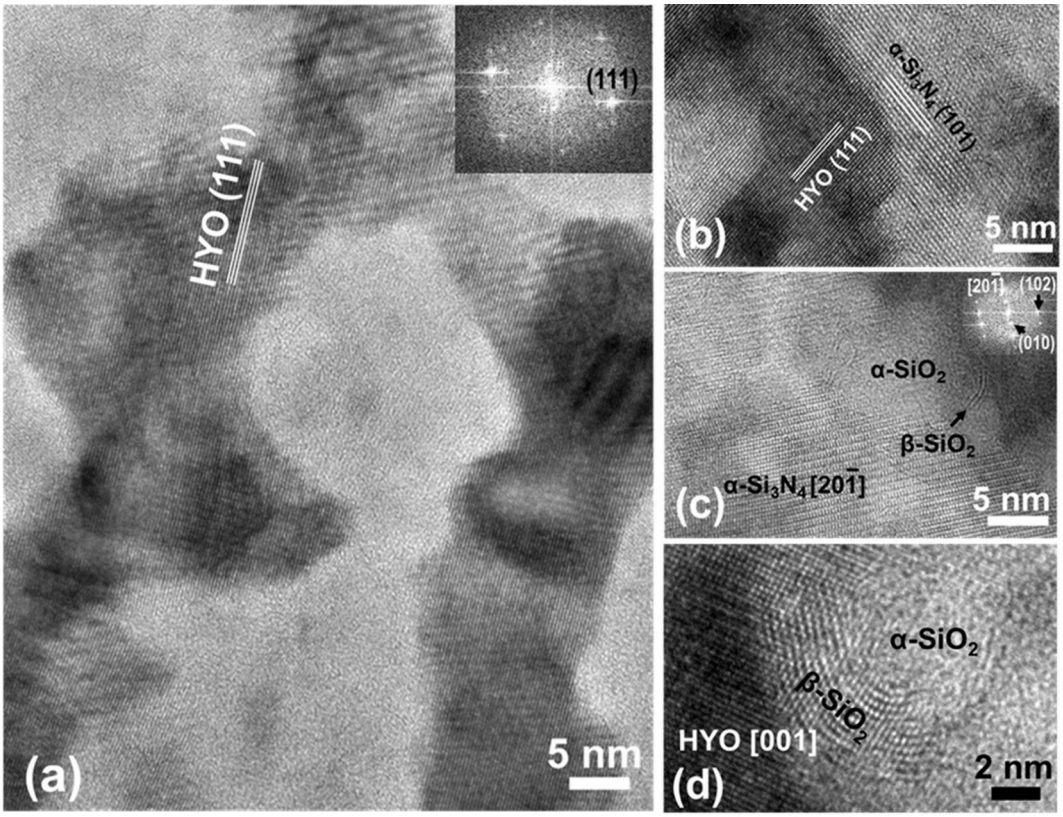

Fig. 6. Cross-section HRTEM images from different region in the TL of the annealed $Hf_6B_{12}Si_{29}Y_2C_2N_{45}$ film exhibiting (a) single oriented fluorite HYO, (b) coexistence of Si_3N_4 and HYO, (c) and (d) mixture of Si_3N_4, β-quartz SiO_2 and amorphous SiO_x (a-SiO_2).

grains. This evidence shows that initiation of oxidation of Si_3N_4 via a sequence of β-SiO_2 and amorphous SiO_x takes place in the top RL section. Investigations of numerous HRTEM images over a large area show that HYO and Si_3N_4 structures were frequently observed, while the HfYCN phase was not observed in the top section of RL in agreement with the electron diffraction analysis in Fig. 7(d). A HRTEM image from the middle section is shown in Fig. 8(b) presenting Si_3N_4, HfYCN, and HYO grains. The (1 1 1) lattice fringes of HfYCN have a spacing of 2.62 Å and those of HYO 2.96 Å. The size of the grains in this region is about ~ 15–20 nm indicating the initial stages of HYO formation. A HRTEM image from the bottom section of the RL (~300 nm above the substrate) is shown in Fig. 8(c) presenting Si_3N_4 and HfYCN grains with a size of ~ 15 nm and ~ 5–10 nm, respectively. These two phases nucleated in the bottom layer followed by grain growth in the middle section, Fig. 8(b), due to the thermal gradient. It is noted that small HYO grains (~5 nm) were rarely observed in this layer indicating some sparse nucleation of HYO.

Fig. 9 shows a HRTEM image from the SiC substrate/film interface. A sharp interface is evident along with formation of Si_3N_4, HfYCN (1 1 1) grains, and HfB_2 strips with their (0 0 1) attached to the SiC substrate. The formation of Si_3N_4, HfB_2 and HfYCN phases close to the SiC substrate is most likely caused by a thermal transport effect [26] from the SiC substrate resulting in localized partial recrystallization.

Based on the above observations, the microstructure development within the RL in the annealed $Hf_6B_{12}Si_{29}Y_2C_2N_{45}$ film can be summarized as follows: (i) during recrystallization, Si and N form a textured Si_3N_4 structure over the entire sublayer, while Hf, Y, and the remaining N form HfYCN in the bottom section followed by grain coarsening in the middle section (up to 850 nm from the substrate); (ii) oxidation of HfYCN and formation of HYO initiates in the middle RL section and progresses more than likely to completion in the top RL section. Gradual coarsening of Si_3N_4 and HYO takes place in this section developing the honeycomb-like nanostructures consisting of Si_3N_4 core enclosed by HYO large nanostructures in the top section; and (iii) initiation of Si_3N_4 oxidation takes place in the top RL section via a sequence of β-SiO_2 formation and amorphous SiO_x.

3.3. Microstructure of annealed $Hf_5B_{13}Si_{25}Ho_3C_2N_{48}$

3.3.1. Overall film structure

Cross-section TEM investigations show that the annealed $Hf_5B_{13}Si_{25}Ho_3C_2N_{48}$ film exhibits a similar multi-layered structure to that of the annealed $Hf_6B_{12}Si_{29}Y_2C_2N_{45}$ film. The film has a thickness of 2280 nm and is composed of a ~ 190 nm thick nanocomposite OL with spherical nanoparticles dispersed in an amorphous SiO_x-based matrix on the top followed by a ~ 300 nm TL of vertically oriented columnar structure and a ~ 1780 nm RL underneath, Fig. 10(a). The RL layer clearly exhibits a graded microstructure with a fine grain structure at the bottom that gradually coarsens as the TL layer is approached.

3.3.2. Microstructure of the top oxide layer and the transition layer

Fig. 10(b) and (c) show plan-view TEM images of the OL and TL in the annealed $Hf_5B_{13}Si_{25}Ho_3C_2N_{48}$ film. Fig. 10(b) was obtained by removing the SiC substrate and the bottom layers and exhibits a typical OL microstructure over a large area within the film plane. Spherical nanoparticles 30 nm to ~ 170 nm in size containing Hf, Ho and O are well-dispersed in SiO_2 amorphous structure. Electron diffraction analysis determined that the $Hf_{1-x}Ho_xO_{2-x/2}$ nanoparticles have a fluorite type structure with a lattice constant of 5.20 Å, similar to that of HYO. The top half SAED pattern in Fig. 10(d) was obtained from the OL in a plan-view TEM foil. The sharp diffraction rings μ, ν, ο, and π having a lattice spacing of 3.00 Å, 2.60 Å, 1.84 Å, and 1.57 Å, were identified to correspond to the (1 1 1), (2 0 0), (2 2 0) and (3 1 1), respectively of a fluorite $Hf_2Ho_2O_7$ phase.

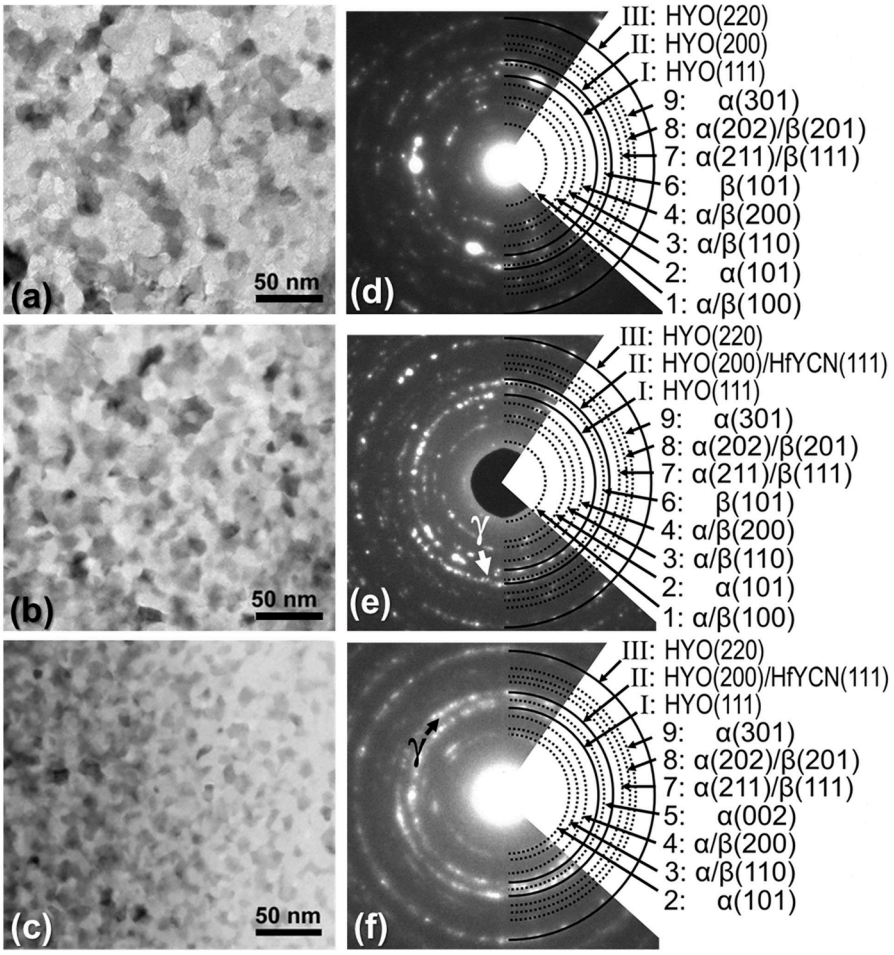

Fig. 7. Cross-section TEM images and SAED patterns from the top (a, d), middle (b, e) and bottom (c, f) section of the RL in the annealed $Hf_6B_{12}Si_{29}Y_2C_2N_{45}$ film.

The TL microstructure obtained by removing the top OL layer, the substrate, and the bottom layer is shown in a plan-view TEM image in Fig. 10(c). It presents a similar morphology to the TL layer in the annealed $Hf_6B_{12}Si_{29}Y_2C_2N_{45}$ film. The dark island-like structures or particles contain O, Hf and Ho, and are linked together forming worm-like, 15–20 nm thick chain structures. The bright regions between the dark chains have a size from 40 to 150 nm and consist of N, O, Si, Hf and Ho, as identified by EDS.

A SAED pattern from the TL layer in Fig. 10(c) is shown at the bottom half of Fig. 10(d). The diffraction rings overlapping with solid dark circles μ, ν, ο, and π, correspond respectively to the (111), (200), (220), and (311) of hafnia holmium fluorite phase that has a lattice constant of 5.14 Å. The HHO in the TL has a smaller lattice constant than the spherical particles in the OL, like the HYO in the annealed $Hf_6B_{12}Si_{29}Y_2C_2N_{45}$ film.

Besides HHO, diffractions from α-Si_3N_4 and β-Si_3N_4 were also seen in the SAED pattern from the TL, as shown in Fig. 10(d). Some diffraction rings (1, 3, 4, 7, 8 and 10) in Fig. 10(d) correspond to the overlapping diffractions from both α- and β-Si_3N_4 phases, while rings 2, 5 and 9 belong only to α-Si_3N_4, and ring 6 only to β-Si_3N_4. The presence of unique (non-overlapping) diffractions (101), (002) and (301) of α-Si_3N_4 and (101) of β-Si_3N_4 indicate that both α-Si_3N_4 and β-Si_3N_4 were formed in the TL layer.

3.3.3. *Microstructure of the recrystallized layer*

The RL underneath the TL appears as a graded nanocomposite structure of dark and bright domains, similar in appearance to the structure observed in the annealed $Hf_6B_{12}Si_{29}Y_2C_2N_{45}$ film. As can be seen from Fig. 10(a), the RL layer clearly presents a distinct graded morphology with densely packed small grains at the bottom section that progressively coarsen. Magnified cross-section TEM images from the top and bottom RL sections with clearly presented detailed microstructure are shown Fig. 11(a, and b). The bottom sublayer is ~ 480 nm thick and consists of a nearly even sized (~10 nm) dark and bright domains (Fig. 11(b)), while the top sublayer presents honeycomb-like structures of substantially grown grains with a size up to 30 nm or even bigger (Fig. 11(a)). The dark structures in the top sublayer were clearly separated by the bright matrix.

The SAED pattern from the top sublayer in Fig. 11(c) shows the presence of α-Si_3N_4, β-Si_3N_4, HHO, and possibly HfCN phases. For example, diffractions μ, ν, ο, and π with a lattice spacing of 2.97 Å, 2.57 Å, 1.81 Å, and 1.55 Å, correspond to (111), (200), (220), and (311), respectively of HHO (lattice constant 5.14 Å). The diffraction spots 2 and x having a lattice spacing of 4.32 and 2.22 Å correspond, respectively, only to the (101) and (300) of α-Si_3N_4, while the spots on ring 6 of 2.66 Å only to the (101) of β-Si_3N_4. The diffraction spots 3, 4, 7, and 8 having a lattice spacing of 3.88 Å, 3.31 Å, 2.32 Å, and 2.17 Å, match, respectively, the (110), (200), (211) and (202) of α-Si_3N_4, or the (110), (200), (111) and (201) of β-Si_3N_4.

The SAED pattern from the bottom recrystallized sublayer in Fig. 11 (d) shows mainly the presence of α-Si_3N_4, and HfCN phases. The diffractions on rings δ, ε, and ϕ with a lattice spacing of 2.62 Å, 2.27 Å, and 1.60 Å, correspond to the (111), (200), and (220) of HfCN, respectively. These lattice spacings are the same to those of HfYCN and can be attributed to incorporation of Ho in the HfCN structure, HfHoCN. Furthermore, it is noted that as in the HfHoCN case, Ho was present in

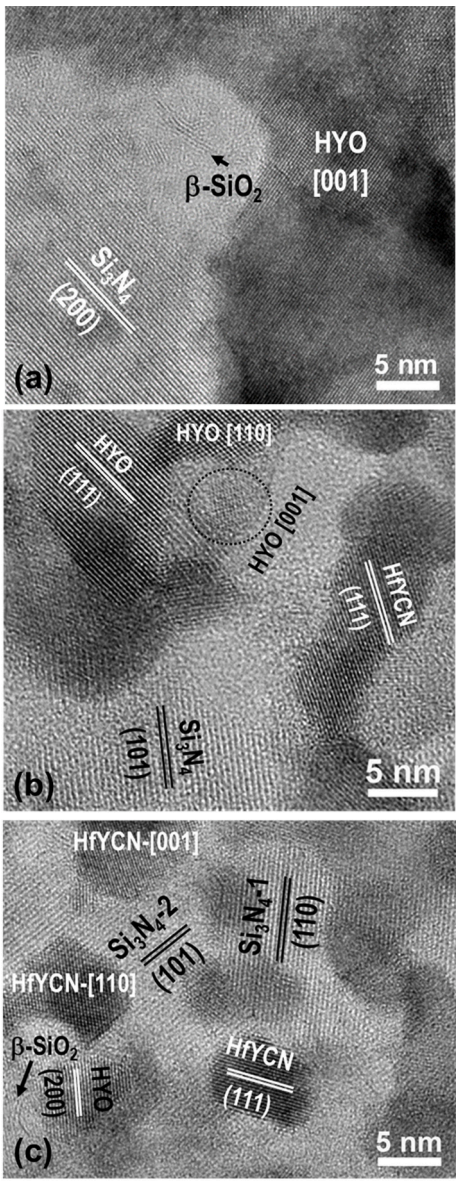

Fig. 8. Cross-section HRTEM images from the (a) top, (b) middle, and (c) bottom section of the RL in the annealed $Hf_6B_{12}Si_{29}Y_2C_2N_{45}$ film.

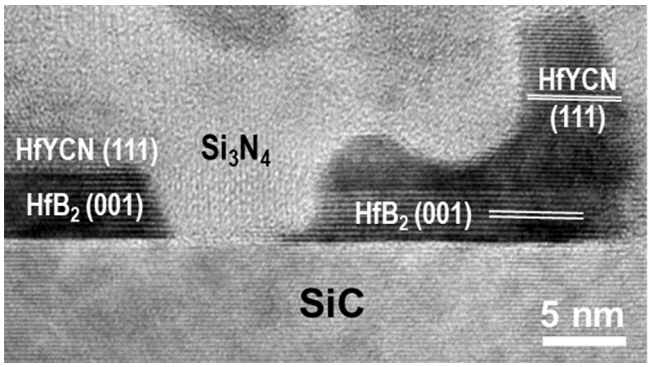

Fig. 9. Cross-section HRTEM image of the RL/SiC substrate interface.

the HHO particles that resulted directly from oxidation of the HfHoCN phase. The β-Si_3N_4 structure was not observed, while the α-Si_3N_4 structure was formed in a highly texture structure in this sublayer. Diffractions from HHO were rarely (if at all) observed. The evidence shows that the HfHoCN phase was formed in the bottom sublayer (up to 480 nm above the substrate) and gradually oxidized forming HHO in the top sublayer.

The detailed microstructure of the upper part of the RL was studied by HRTEM. Fig. 12(a) shows a magnified TEM image, in which the dark HHO grains have almost polygonal shape with very clear edges and sharp tips. The tips are connected to the boundaries (marked by arrows) between Si_3N_4 grains. The boundaries between Si_3N_4 grains possess stronger contrast compared to the pale Si_3N_4 grains (~10 nm) and are interconnected to form a boundary network. The network boundaries surrounding Si_3N_4 (denoted also as SN) grains in Fig. 12(a) are thin layers of either high temperature, β-quartz SiO_2 (PDF #11–0252, a = 5.002 Å, c = 5.454 Å, P3221), as evidenced by the presence of curved (1 0 1) lattice fringes with a spacing of ~ 3.4 Å in Fig. 12(b), or amorphous, such as marked by $B_{1,2}$, $B_{1,3}$ and $B_{2,3}$ between three silicon nitride grains Si_3N_4-1, Si_3N_4-2 and Si_3N_4-3 in Fig. 12(c). The amorphous boundaries are most likely composed of silicon oxide. These results indicate that the oxidation of Si_3N_4 was initiated at Si_3N_4 grain boundaries. Fig. 12(d) is a HRTEM image from a different area of the upper section of the RL presenting coexistence of HHO and HfHoCN grains. Fig. 12(d) also presents the coexistence of α-Si_3N_4 ($d_{(1\,0\,1)}$ = 4.34 Å) and β-Si_3N_4 ($d_{(1\,0\,1)}$ = 2.66 Å). Intensive studies showed that HHO and α-Si_3N_4 phases dominated the upper section of the RL layer, while the HfHoCN and β-Si_3N_4 were also present but at a smaller extent.

Examination of the lower RL section revealed a partially recrystallized microstructure, Fig. 13, composed mainly of HfHoCN and α-Si_3N_4 while the HHO was rarely observed. The grains of these phases exhibited smooth boundaries with direct evidence of interconnected fringes suggesting a smooth recrystallization process of the original amorphous film structure. Finally, the annealed $Hf_5B_{13}Si_{25}Ho_3C_2N_{48}$ film exhibited a sharp interface with the SiC substrate like that observed in the Y doped film.

Therefore, the microstructure development within the RL in the annealed $Hf_5B_{13}Si_{25}Ho_3C_2N_{48}$ film can be summarized as follows: (i) during annealing, bonding of Si and N forms a Si_3N_4 textured structure over the entire sublayer, while Hf, Ho and the remaining N form HfHoCN; (ii) progressive oxidation of HfHoCN and formation of HHO initiates at the upper RL section. As a result, the portion of HfHoCN is gradually decreasing along this section while that of HHO increases. The fine HfHoCN and α-Si_3N_4 grain structure in the lower RL section is accompanied by coarsening and concomitant gradual transformation (oxidation) of HfHoCN to HHO along with formation of β-Si_3N_4 developing a honeycomb-like microstructure. At the same time, oxidation of Si_3N_4 initiates at the upper RL section via formation of β-SiO_2 first followed by transformation of the latter phase into amorphous SiO_x.

4. Discussion

The as-deposited amorphous $Hf_6B_{12}Si_{29}Y_2C_2N_{45}$ and $Hf_5B_{13}Si_{25}Ho_3C_2N_{48}$ films have been found to be optically transparent, thermally stable and oxidation resistant in air up to 1300 °C [33]. Annealing experiments in inert gasses have shown that the crystallization of the amorphous structure occurs at approximately 1400 °C [33]. Thus, exposure of these films in air above 1400 °C involves oxidation of the recrystallized structure. The $Hf_6B_{12}Si_{29}Y_2C_2N_{45}$ and $Hf_5B_{13}Si_{25}Ho_3C_2N_{48}$ annealed films exhibit a similar overall structural morphology to the undoped $Hf_7B_{10}Si_{32}C_2N_{44}$ film [1] due to a very similar composition, but with some distinct differences in their detailed microstructure arising from the Y or Ho doping.

At around 1400 °C, the amorphous structure becomes unstable, and initiation of diffusion processes promotes segregation and formation of α-/β-Si_3N_4 and fcc Hf(Y/Ho)CN in the RL. It is noted that previous studies showed that Y doped ZrN (similar nitride to HfN) could maintain the ZrN crystalline structure with minor unit cell dimension changes without the presence of second phase and maintained a stoichiometric

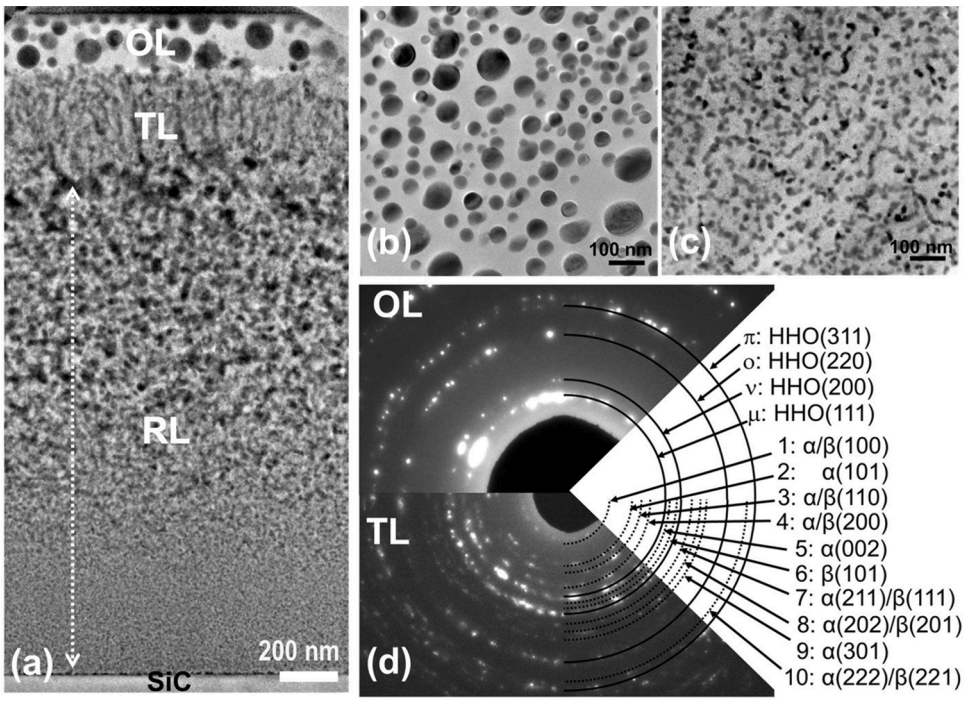

Fig. 10. (a) Cross-section TEM image of the annealed $Hf_5B_{13}Si_{25}Ho_3C_2N_{48}$ film; Plan-view TEM image of the (b) OL, and (c) TL. (d) A superposition of SAED patterns of the OL and the TL in a plan-view TEM foil.

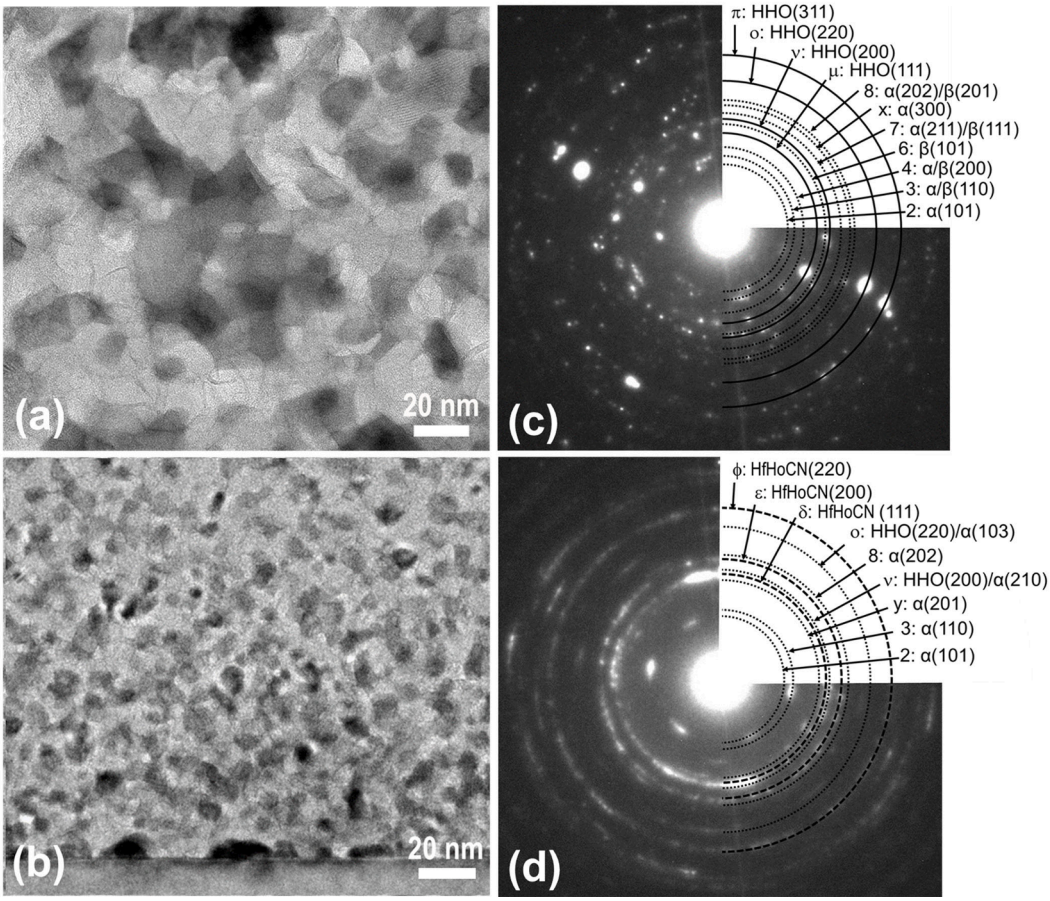

Fig. 11. Cross-section TEM images and SAED patterns from the top (a, c) and bottom (b, d) section of the RL in the annealed $Hf_5B_{13}Si_{25}Ho_3C_2N_{48}$ film.

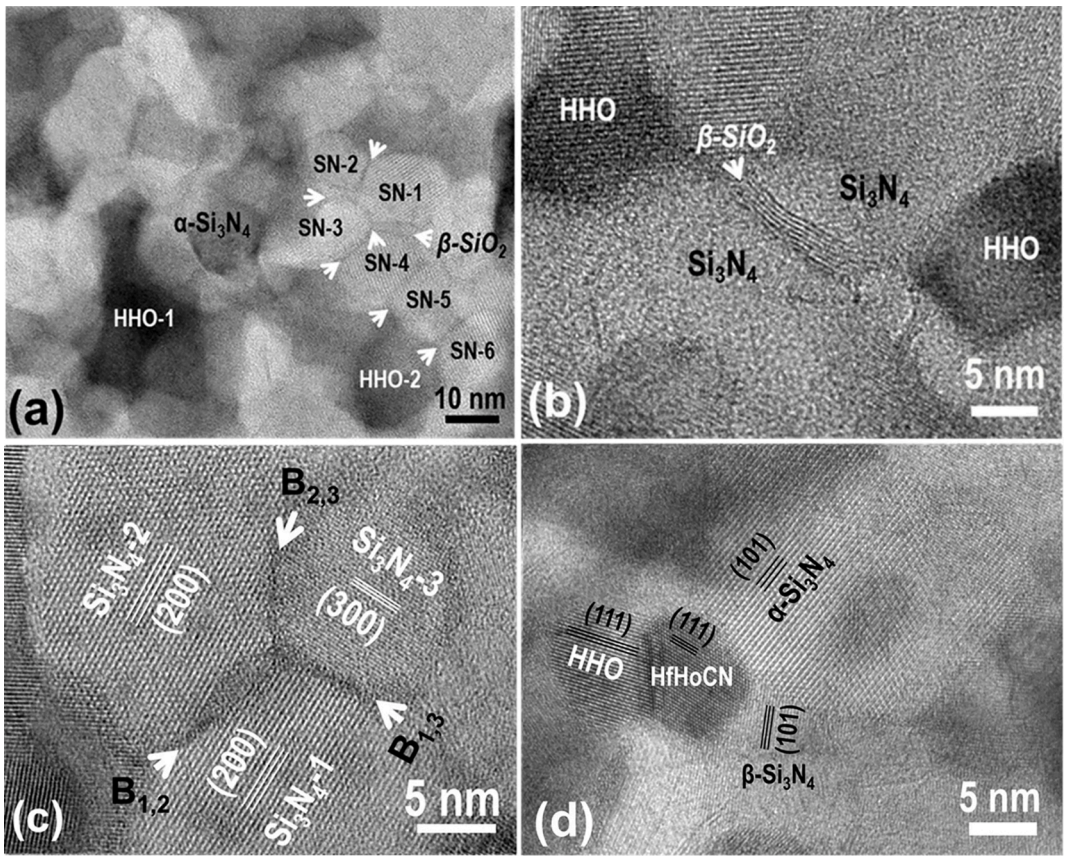

Fig. 12. (a) A zoom-in cross-section TEM image, and (b-d) cross-section HRTEM image from different areas in the upper RL section in the annealed $Hf_5B_{13}Si_{25}$-$Ho_3C_2N_{48}$ film.

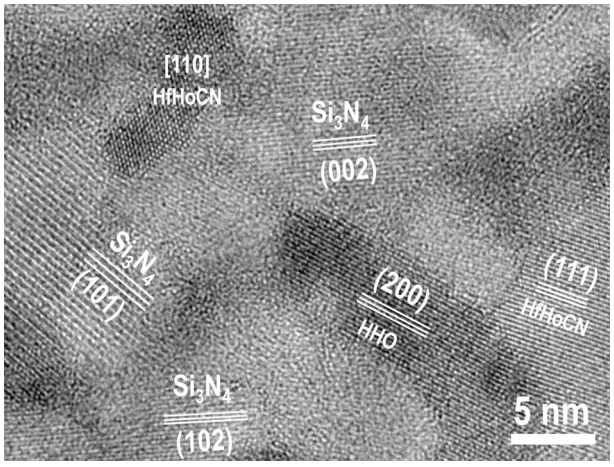

Fig. 13. Cross-section HRTEM image from the lower RL section.

N/(Zr + Y) ratio of 1:1 [38,39]. Only very limited studies have focused on the Hf(Y)N or Hf(Ho)N system, but based on the present evidence, it is reasonable to argue that they share similarities with Zr(Y)N, i.e., Y and Ho can form rare earth Hf(Y)N and Hf(Ho)N mononitrides with fcc NaCl crystal structure, which is the same as HfN despite a slight variation in the lattice parameter [40]. It is worth noting, that intimate, atomically sharp Hf(Y/Ho)CN/Si_3N_4 interfaces were observed in the RL but also between all phases in the rest two layers indicative of high density and film quality, Fig. 8(c) and 12(d).

At the lower part of the RL, a fine gradient microstructure with a grain size 10–15 nm evolves, composed of Si_3N_4 and Hf(Y/Ho)CN, Figs. 7 and 11, followed by grain coarsening at the upper parts of this layer. Several interesting observations were made in this layer as its upper part is approached. First, starting from the middle part of the RL, the Hf(Y/Ho)CN phase gradually oxidized to form H(Y/H)O with the fraction of the former decreasing and the latter increasing as the RL/TL interface is approached. This process resulted in a microstructure composed of Si_3N_4 and a honeycomb-like structure of merged H(Y/H)O nanoparticles. Second, limited oxidation of Si_3N_4 initiated at the upper RL part close to the RL/TL interface. These observations captured the very first stages of the Si_3N_4 oxidation mechanism that involves initial formation of β-SiO_2 at Si_3N_4 grain boundaries and its subsequent transformation to amorphous SiO_x. As note earlier, in all the above oxidation processes seamless, atomically sharp interfaces are produced between H(Y/H)O/Si_3N_4 and H(Y/H)O/SiO_2/ Si_3N_4, Figs. 6 and 12.

Our observations further revealed that the presence of H(Y/H)O was detected deeper in the RL where limited oxidation of Si_3N_4 was observed only at the upper part of RL. This indicates that as O diffuses in the RL, reacts preferentially with Hf in Hf(Y/Ho)CN forming H(Y/H)O than reacting with Si in Si_3N_4. The preferential oxidation of Hf atoms is also supported by considering the lower free energy of oxide formation for Hf compared to Si [27].

The partial oxidation in the RL was found to be more extensive in the Ho-doped compared to Y-doped film. However, both Y- and Ho– doped annealed films exhibited somewhat more oxidation than the undoped $Hf_7B_{10}Si_{32}C_2N_{44}$ film. This is possibly because the Hf-Y-O and Hf-Ho-O fluorite is an oxygen-deficient structure since Y^{3+} and Ho^{3+} substitute Hf^{4+} creating extra oxygen vacancies which facilitates faster oxygen diffusion and oxidation.

Crossing into the TL, H(Y/H)O nanoparticles coarsen and merge together forming a well-developed shell structure of vertically oriented nanocolumns with (1 1 1) preferred crystallographic orientation, Fig. 2

(a) and 10(a). The regions (~40–200 nm in size) surrounded by the H(Y/H)O shells consist of large Si_3N_4 domains, some β-SiO_2 and amorphous SiO_x along with dispersed H(Y/H)O nanodomains. Such vertically oriented (1 1 1) H(Y/H)O nanocolumnar structure has not been observed previously in the absence of rare earth additions in Hf-Si-B-C-N films. As noted earlier, Y and Ho additions in the present films can generate extra oxygen vacancies in their structure. It is plausible that oxygen vacancies are preferentially located on high density (1 1 1) planes to release strain causing crystallographic preferential oxidation. It is important to note that our observations show that most of the regions surrounded by the H(Y/H)O were occupied by large Si_3N_4 grains with limited SiO_2 formation. Extensive oxidation of Si_3N_4 did not take place beyond that observed in the upper part of the RL. This clearly shows that in most of its part, Si_3N_4 remains resistant to oxidation in the TL.

At the TL/OL interface, shown in the lower part of Fig. 3(a), Si_3N_4 oxidizes and the top fully OLs of both annealed films compose of an amorphous SiO_x-based matrix with dispersed large, spherical cubic fluorite oxide H(Y/H)O nanoparticles. It can be envisioned that as the Si_3N_4 grains oxidize forming amorphous SiO_x, the surrounding H(Y/H)O columns breakdown producing spherical H(Y/H)O oxide nanoparticles. The OLs in the two doped films have nearly the same thickness of ~ 190 nm, which is about 36 % thinner than the one in the undoped $Hf_7B_{10}Si_{32}C_2N_{44}$ film [1]. This indicates that addition of Y or Ho to Hf-B-Si-C-N films significantly reduces the thickness of the fully oxidized layer on the surface.

The presence of cubic fluorite oxide H(Y/H)O observed in the present Y/Ho-doped films contrasts with the monoclinic and orthorhombic HfO_2 nanoparticles reported previously in the undoped Hf-B-Si-C-N films [1,25,27]. Typically, cubic hafnium oxide is only stable at temperatures higher than 2500 °C [41,42]. However, by adding some of the rare earth elements, Hf may be able to form a Hf-RE-O solid solution that closely resembles the crystalline structure of fluorite or pyrochlore at lower temperatures [43–48]. For example, 5 mol% Y doping to the Hf-Y-O system would maintain the cubic HfO_2 at 2000 °C and 10 mol% Y at 1200 °C [43]. This is because, as Y randomly substitutes Hf within the lattice, the charge neutrality is preserved by forming an anion vacancy defect structure. Such types of solid solution were also called rare earth elements stabilized hafnia. It was found that Y and Ho can form only fluorite oxide with HfO_2 while some other elements such as La could form pyrochlore structure ($La_2Hf_2O_7$). As concentration of Y and Ho increases, the unit cell dimensions of these fluorite oxides also increase. For example, the unit cell of HYO is around 5.13 x 5.13 x 5.13 $Å^3$ when Y_2O_3 reaches 10 mol% and increases to almost 5.22 x 5.22 x 5.22 $Å^3$ when Y_2O_3 concentration increased to 40 mol% [43]. Similar trend has been observed in the HHO system as well. This is mostly due to larger ion radius of Y^{3+} and Ho^{3+} compared to Hf^{4+}[44]. No traces of Y_2O_3 or Ho_2O_3 phases were found in the annealed $Hf_6B_{12}Si_{29}Y_2C_2N_{45}$ and $Hf_5B_{13}Si_{25}Ho_3C_2N_{48}$ films. This indicates that all oxidized Y and Ho in the doped films has been involved into HYO and HHO fluorite oxides.

It should be further noted that the Gibbs free energy of formation for SiO_2 at 1800 K is reported as −579 kJ/mol [49]. In contrast, the predicted Gibbs free energy of formation for monoclinic and tetragonal HfO_2 at 1773 K is −211,493.4 kJ/mol and −202,839.6 kJ/mol, respectively [50]. Although the free energies of formation for H(Y/H)O are not provided in the referenced paper, it is speculated that these values are likely to be close to those of HfO_2. Notably, these values are considerably lower when compared to the corresponding value for SiO_2. This observation aligns with the finding that, as oxygen diffuses in the RL layer, it tends to preferentially react with Hf in Hf(Y/Ho)CN, forming H(Y/H)O, rather than reacting with Si in Si_3N_4.

5. Conclusions

The microstructure of the $Hf_6B_{12}Si_{29}Y_2C_2N_{45}$ and $Hf_5B_{13}Si_{25}Ho_3C_2N_{48}$ films annealed up to 1500 °C in air exhibited a similar three-layered structure morphology consisting of: (i) a top fully oxidized layer composed of a dispersion of cubic fluorite H(Y/H)O nanoparticles embedded in an amorphous SiO_x-based matrix followed by (ii) a transition layer of vertically oriented nanocolumnar orientation preferred H(Y/H)O nanostructure network surrounded by Si_3N_4 domains and (iii) a bottom recrystallized nanostructured layer composed of Si_3N_4 and Hf(Y/Ho)CN in its lower part with the Hf(Y/Ho)CN gradually oxidizing to H(Y/H)O in its upper section along the thickness of the layer. Hf(Y/Ho)CN was fully oxidized in the transition layer.

Initial stages of oxidation of Si_3N_4 were observed in the upper part of the recrystallized layer that continued in into the transition layer. The oxidation process involved first formation of β-SiO_2 and its subsequent transformation to amorphous SiO_x. The thickness of the oxidized layer (~190 nm) was found to be about 36 % thinner than the one in the undoped Hf-B-Si-C-N films of similar composition. Intimate, atomically sharp interfaces were observed between all phases in the annealed films indicative of high density and film quality. The Y- and Ho– doping was found to stabilize the cubic fluoride oxide H(Y/H)O structure and promote its columnar texture.

CRediT authorship contribution statement

J.C. Jiang: Investigation, Methodology, Data curation, Validation, Writing – original draft. **Y. Shen:** . **P. Zeman:** . **M. Procházka:** . **J. Vlček:** Conceptualization. **E.I. Meletis:** Funding acquisition, Supervision, Validation, Writing – review & editing.

Declaration of competing interest

The authors declare that they have no known competing financial interests or personal relationships that could have appeared to influence the work reported in this paper.

Data availability

Data will be made available on request.

Acknowledgments

This work was supported by the U.S. National Science Foundation under Award No. NSF/DMR 2122128 and by the ERDF (Ministry of Education, Youth and Sports, Czech Republic) project QM4ST with No. CZ.02.01.01/00/22_008/0004572.

References

[1] Y. Shen, J. Jiang, P. Zeman, M. Kotrlová, V. Šímová, J. Vlček, E.I. Meletis, Microstructure of high temperature oxidation resistant $Hf_6B_{10}Si_{31}C_2N_{50}$ and $Hf_7B_{10}Si_{32}C_2N_{44}$ films, Coatings 10 (12) (2020) 1170.
[2] C. Mitterer, Borides in thin film technology, J. Solid State Chem. 133 (1997) 279–291.
[3] M.M. Opeka, I.G. Talmy, E.J. Wuchina, J.A. Zaykoski, S.J. Causey, Mechanical, thermal, and oxidation properties of refractory hafnium and zirconium compounds, J. Eur. Ceram. Soc. 19 (1999) 2405–2414.
[4] M.M. Opeka, I.G. Talmy, J.A. Zaykoski, Oxidation-based materials selection for,, °C + hypersonic aerosurfaces: theoretical, J. Mater. Sci. 9 (2004) (2000) 5887–5904.
[5] E. Opila, S. Levine, J. Lorincz, Oxidation of ZrB2- and HfB2-based ultra-high temperature ceramics: effect of Ta additions, J. Mater. Sci. 39 (2004) 5969–5977.
[6] S.R. Levine, E.J. Opila, M.C. Halbig, J.D. Kiser, M. Singh, J.A. Salem, Evaluation of ultra-high temperature ceramics for aeropropulsion use, J. Eur. Ceram. 22 (14–15) (2002) 2752–2756.
[7] W.G. Fahrenholtz, G.E. Hilmas, Ultra-high temperature ceramics: materials for extreme environment, Scr. Mater. 129 (2017) 94–99.
[8] W.G. Fahrenholtz, G.E. Hilmas, I.G. Talmy, J.A. Zaykoski, Refractory diborides of zirconium and hafnium, J. Am. Ceram. Soc. 90 (2007) 1347–1364.
[9] E. Wuchina, E. Opila, M. Opeka, W. Fahrenholtz, I. Talmy, UHTCs: ultra-high temperature ceramic materials for extreme environment applications, Electrochem. Soc. Interface 16 (2007) 30–36.
[10] F. Monteverde, The thermal stability in air of hot-pressed diboride matrix composites for uses at ultra-high temperatures, Corros. Sci. 47 (2005) 2020–2033.
[11] F. Monteverde, A. Bellosi, The resistance to oxidation of an HfB_2-SiC composite, J. Eur. Ceram. Soc. 25 (2005) 1025–1031.

[12] F. Monteverde, A. Bellosi, L. Scatteia, Processing and properties of ultra-high temperature ceramics for space applications, Mater. Sci. Eng. A 485 (2008) 415–421.
[13] D. Ghosh, G. Subhash, Recent progress in Zr(Hf)B2 based ultrahigh temperature ceramics in Handbook of Advanced Ceramics (2nd Edition), Materials, Processing, and Properties, Academic Press, Applications, 2013.
[14] E. Zapata-Solvas, D.D. Jayaseelan, H.T. Lin, P. Brown, W.E. Lee, Mechanical properties of ZrB_2- and HfB_2- based ultra-high temperature ceramics fabricated by spark plasma sintering, J. Eur. Ceram. Soc. 33 (2013) 1373–1386.
[15] C.M. Carney, Oxidation resistance of hafnium diboride-silicon carbide from 1400 to,, °C, J. Mater. Sci. 44 (2009) (2000) 5673–5681.
[16] C.M. Carney, P. Mogilvesky, T.A. Parthasarathy, Oxidation behavior of zirconium diboride silicon carbide produced by the spark plasma sintering method, J. Am. Ceram. Soc. 92 (2009) 2046–2052.
[17] M. Zhang, J. Jiang, J. Houška, J. Kohout, J. Vlček, E.I. Meletis, A study of the microstructure evolution of hard Zr–B–C–N films by high-resolution transmission electron microscopy, Acta Materialia 77 (2014) 212–222.
[18] J. He, M.H. Zhang, J.C. Jiang, J. Vlček, P. Zeman, P. Steidl, E.I. Meletis, Microstructure characterization of high-temperature, oxidation-resistant Si-B-C-N films, Thin Solid Films 542 (2013) 167–173.
[19] M. Mallik, K.K. Ray, R. Mitra, Oxidation behavior of hot pressed ZrB_2-SiC and HfB_2-SiC composites, J. Eur. Ceram. Soc. 31 (2011) 199–215.
[20] F. Menteverde, Progress in Fabrication of Ultra-high temperature Ceramics: "in situ" synthesis, microstructure and properties of a reactive hot-pressed HfB_2-SiC composite, Comp. Sci. Tech. 65 (2005) 1869–1879.
[21] F. Menteverde, A. Bellosi, The resistance to oxidation of an HfB_2-SiC composite, J. Euro. Ceram. Soc. 25 (2008) 1025–1031.
[22] J. Čapek, S. Hřeben, P. Zeman, J. Vlček, R. Čerstvý, J. Hruska, Effect of the gas mixture composition on high-temperature behavior of magnetron sputtered Si-B-CN coatings, Surf. Coat. Technol. 203 (2008) 466–469.
[23] M.H. Zhang, J.C. Jiang, E.I. Meletis, P. Mares, H. J., J. Vlček,, Effect of the Si Content on the Microstructure of Hard, Multifunctional Hf-B-Si-C Films Prepared by Pulsed Magnetron Sputtering, Appl. Surf. Sci. 357 (2015) 1343–1354.
[24] P. Zeman, J. Čapek, R. Čerstvý, J. Vlček, Thermal stability of magnetron sputtered Si-B-C-N materials at temperatures up to 1700°C, Thin Solid Films 519 (2010) 306–311.
[25] Y. Shen, J.C. Jiang, P. Zeman, V. Šímová, J. Vlček, E.I. Meletis, Microstructure Evolution in Amorphous Hf-B-Si-C-N High Temperature Resistant Coatings after Annealing to 1500 °C in Air, Scientific Reports 9 (2019) 3603.
[26] P. Zeman, Š. Zuzjaková, P. Mareš, R. Čerstvý, M.H. Zhang, J.C. Jiang, E.I. Meletis, J. Vlček, Superior High-temperature Oxidation Resistance of Magnetron Sputtered Hf–B–Si–C–N Film, Ceram. Int. 42 (2016) 4853–4859.
[27] M.H. Zhang, J.C. Jiang, P. Zeman, Š. Zuzjaková, J. Vlček, E.I. Meletis, Study of the High-temperature Oxidation Resistance Mechanism of Magnetron Sputtered $Hf_7B_{23}Si_{17}C_4N_{45}$ Film, J. Vac. Sci. Technol. A 36 (2018), 021505.
[28] K.N. Lee, D.S. Fox, N.P. Bansal, Rare earth silicate environmental barrier coatings for SiC/SiC composites and Si_3N_4 ceramics, Journal of the European Ceramic Society 25 (2005) 1705–1715.
[29] B.-K. Jang, F.-J. Feng, K.-S. Lee, E. García, A. Nistal, N. Nagashima, S. Kim, Y.-S. Oh, H.-T. Kim, Thermal behavior and mechanical properties of Y_2SiO_5 environmental barrier coatings after isothermal heat treatment, Surface and Coatings Technology 308 (2016) 24–30.
[30] M.-H. Lu, H.-M. Xiang, Z.-H. Feng, X.-Y. Wang, Y.-C. Zhou, Mechanical and thermal properties of Yb_2SiO_5: a promising material for T/EBCs applications, J. Am. Ceram. Soc. 99 (4) (2016) 1404–1411.
[31] N.A. Nasiri, N. Patra, D. Horlait, D.D. Jayaseelan, W.E. Lee, Thermal properties of rare-earth monosilicates for EBC on Si-based ceramic composites, J. Am. Ceram. Soc. 99 (2016) 589–596.
[32] Z. Tian, L. Zheng, J. Wang, P. Wan, J. Li, J. Wang, Theoretical and experimental determination of the major thermo-mechanical properties of RE2SiO5 (RE=Tb, Dy, Ho, Er, Tm, Yb, Lu, and Y) for environmental and thermal barrier coating applications, J. Eur. Ceram. Soc. 36 (2016) 189–202.
[33] M. Kotrlová, P. Zeman, J. Houška, V. Šímová, M. Procházka, R. Čerstvý, S. Haviar, J. Vlček, Enhancement of high-temperature oxidation resistance and thermal stability of hard and optically transparent Hf–B–Si–C–N films by Y or Ho addition, Journal of Non-Crystalline Solids 120470 (2020).
[34] International Centre for Diffraction Data, PDF-4 Database Sets, Pennsylvania, USA, 2020.
[35] D.W. Stacy, D.R. Wilder, The Yittria-Hafnia System, Journal of the American Ceramic Society - Foster 58 (1975) 285–288.
[36] H. Toraya, Crystal structure refinement of a-Si_3N_4 using synchrotron radiation powder diffraction data: unbiased refinement strategy, J. Appl. Cryst. 33 (2000) 95–102.
[37] D. du Boulay, N. Ishizawa, T. Atake, V. Streltsov, K. Furuya, F. Munakata, Synchrotron X-ray and ab initio studies of β-Si_3N_4, Acta Cryst. B 50 (2004) 388–405.
[38] Z. Wu, Z. Qi, D. Zhang, Z. Wang, Evolution of the microstructure and oxidation resistance in co-sputtered Zr–Y–N coatings, Appl. Surf. Sci. 321 (2014) 268–274.
[39] J. Musil, H. Poláková, Hard nanocomposite Zr–Y–N coatings, correlation between hardness and structure, Surf. Coat. Technol. 127 (2000) 99–106.
[40] F. Natali, B.J. Ruck, N.O.V. Plank, H.J. Trodahl, S. Granville, C. Meyer, Rare earth mononitrides, Progress in Materials Science 58 (2013) 1316–1360.
[41] O. Ohtaka, H. Fukui, T. Kunisada, H. Fujisawa, Phase relations and volume change of hafnia under high pressure and high temperature, J. Am. Ceram. Soc. 84 (2001) 1369–1373.
[42] T.A. Lee, A. Navrotsky, Enthalpy of formation of cubic yttria-stabilized hafnia, J. Mater. Res. 19 (2004) 1855–1861.
[43] D.W. Stacy, D.R. Wilder, The yttria-hafnia system, J. Am. Ceram. Soc. 58 (1975) 285–288.
[44] V.B. Glushkova, F. Hanic, L.V. Sazonova, Lattice parameters of cubic solid solutions in the systems uR2O3-(1-u)MO2, Ceramurgia International 4 (1978) 176–178.
[45] P. Duwez, F.H. Brown Jr, F. Odell, The zirconia-yttria system, J. Electrochem. Soc. 98 (1951) 356.
[46] C. Li, Y. Ma, Z. Xue, Y. Yang, J. Chen, H. Guo, Effect of Y doping on microstructure and thermophysical properties of yttria stabilized hafnia ceramics, Ceramics International 44 (2018) 18213–18221.
[47] C.K. Roy, M. Noor-A-Alarm, A.R. Choudhuri, C.V. Ramana, Synthesis and microstructure of Gd_2O_3-doped HfO_2 ceramics, Ceram. Int. 38 (2012) 1801–1806.
[48] E.R. Andrievskaya, Phase equilibria in the refractory oxide systems of zirconia, hafnia and yttria with rare-earth oxides, J. Eur. Ceram. Soc. 28 (2008) 2363–2388.
[49] J. Chipman, The free energy of silica, J. Am. Chem. Soc. 83 (1961) 1762–1763.
[50] J.J. Low, N.H. Paulson, M. D'Mello, M. Stan, Thermodynamics of monoclinic and tetragonal hafnium dioxide (HfO2) at ambient pressure, Calphad 72 (2021), 102210.